

Increased rainfall volume from future convective storms in the US

Andreas F. Prein¹*, Changhai Liu, Kyoko Ikeda, Stanley B. Trier, Roy M. Rasmussen, Greg J. Holland and Martyn P. Clark

Mesoscale convective system (MCS)-organized convective storms with a size of ~100 km have increased in frequency and intensity in the USA over the past 35 years¹, causing fatalities and economic losses². However, their poor representation in traditional climate models hampers the understanding of their change in the future³. Here, a North American-scale convection-permitting model which is able to realistically simulate MCSs⁴ is used to investigate their change by the end-of-century under RCP8.5 (ref. ⁵). A storm-tracking algorithm⁶ indicates that intense summertime MCS frequency will more than triple in North America. Furthermore, the combined effect of a 15–40% increase in maximum precipitation rates and a significant spreading of regions impacted by heavy precipitation results in up to 80% increases in the total MCS precipitation volume, focussed in a 40 km radius around the storm centre. These typically neglected increases substantially raise future flood risk. Current investments in long-lived infrastructures, such as flood protection and water management systems, need to take these changes into account to improve climate-adaptation practices.

Economic losses from convective storms are steadily increasing in the USA and currently exceed US\$20 billion annually². Many of these losses are caused by MCSs that produce flash floods, debris flows, landslides, high winds and hail. Flash floods alone cause 84 fatalities per year, which is more than any other weather hazard in the United States, except for heatwaves⁷. A rising frequency and intensity of long-lasting MCSs was found in observations during spring in the Central United States, which led to an increase of subdaily convective rainfall extremes during the past 35 years¹. Australian observations confirm this trend and show that rainfall has become spatially more concentrated over a similar time period⁸. Observed extreme daily precipitation increased in all regions of the United States during the period from 1958 to 2012⁹. Extreme rainfall is expected to increase further by approximately 7% per degree of global warming, which is implied by an increased capacity for water vapour in a warmer atmosphere through considerations from the Clausius–Clapeyron (CC) relationship¹⁰. Such increases are confirmed by observations and model results^{3,11–13}.

Here we use a set of two continuous 13-year long 4 km horizontal grid spacing continental-scale convection-permitting climate model (CPCM) simulations to investigate climate change effects on MCSs during June, July and August (JJA) over North America¹¹. By using a storm-tracking algorithm⁶ we can identify and track MCSs in space and time according to their hourly precipitation fields. The detected MCSs are consistent with standard definitions of contiguous heavy precipitation for a minimum of 100 km in at least one direction¹⁴ and a minimum duration of four hours¹. Also, the

frequency of ~60 MCSs per summer season in the Central United States is similar to that in previous studies^{1,15}. It cannot be ruled out that a small fraction of frontal precipitation is picked up by the tracking algorithm, but this is unlikely to affect the results systematically. A schematic on how MCSs are tracked and how they change in the future period is shown in Fig. 1. The CPCM is able to simulate realistic MCSs (Supplementary Fig. 1) and can reproduce the characteristics of observed MCSs, such as their maximum rain rate, size,

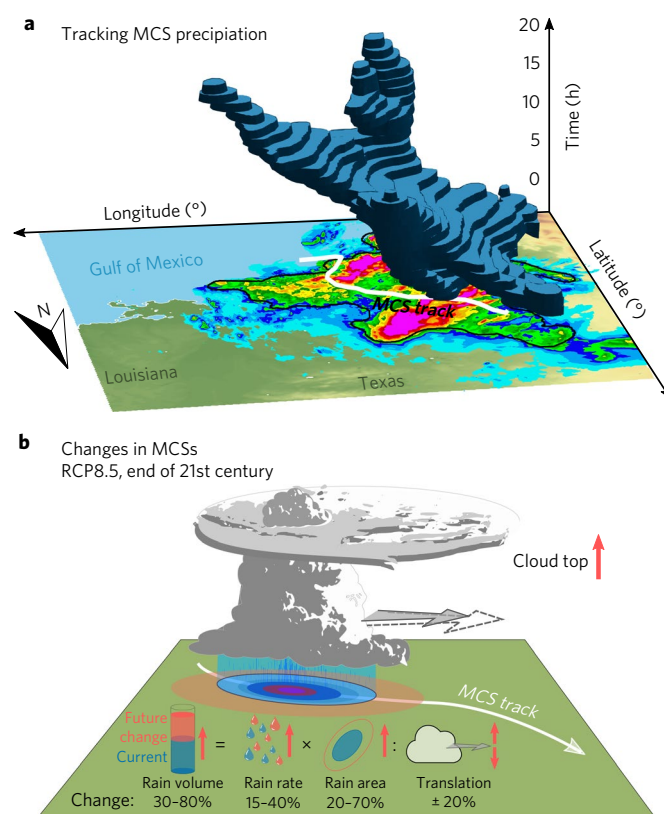


Fig. 1 | Schematic of Lagrangian tracking of MCS precipitation and future changes in MCSs. a, MCS hourly precipitation accumulations above 5 mm h⁻¹ are identified and tracked over space and time (time corresponds to the vertical axis). **b**, Characteristics such as storm motion, rain rates or cloud top heights are identified for MCSs in the current and future climate. Highest increases are found for MCS precipitation volumes, which is positively related to increasing rain rates and rain areas and negatively to changes in storm motion (**b**).

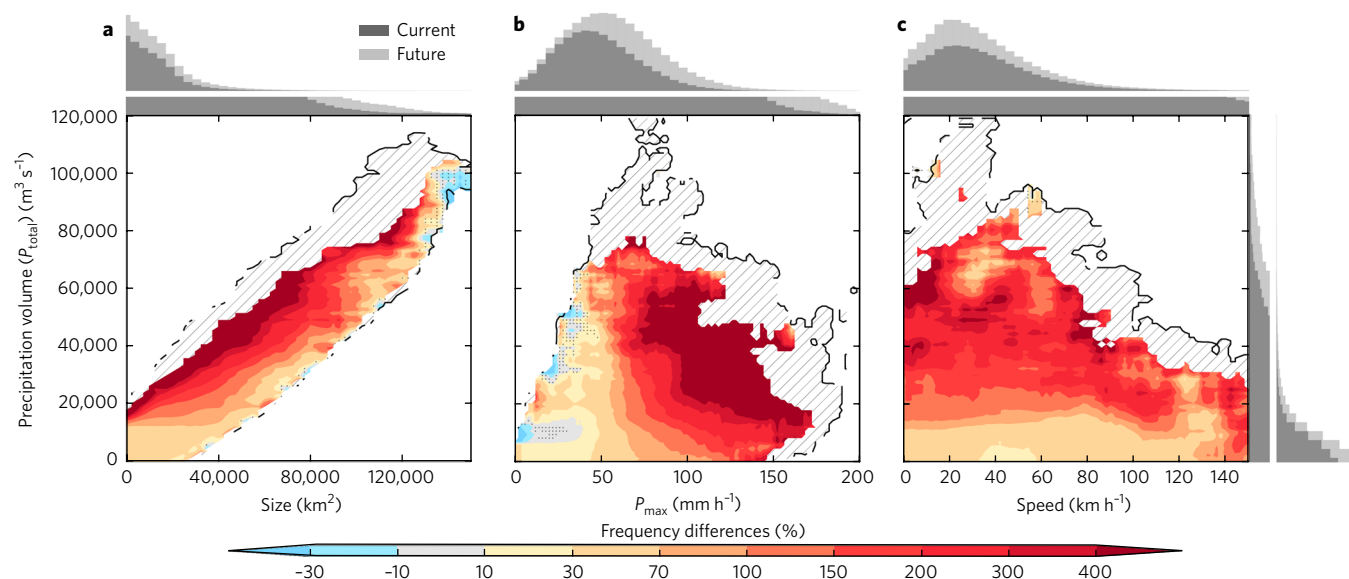


Fig. 2 | Relative frequency changes of MCSs according to their characteristics. **a–c**, Relative differences in the future minus current conditional distribution of MCS size (**a**), P_{\max} (**b**) and storm speed (**c**) conditioned on P_{total} for all MCS hours over land. Filled contour areas correspond to regions with at least five MCSs in the current climate and black hatched contours show areas with at least five MCS hours in the future. Dotted areas show non-significant differences (alpha is 0.1) based on 100 Bootstrap samples. Black/grey bars show current/future empirical density functions for the dimension they are adjacent to. The density functions are split to show the full distributions and a zoom on their tails.

total rainfall and storm motion, within observational uncertainties⁴. However, the frequency of MCSs is up to 50% underestimated in the Central United States and up to 50% overestimated along the Gulf and Atlantic Coast⁵. The Central United States bias results from a systematic underestimation of MCS frequencies in situations with weak synoptic-scale gradients, which is related to a model warm bias during late summer caused by an overestimation of incoming solar radiation and biases in soil–atmosphere interactions⁵. Note that these frequency biases could possibly affect the climate change signals of MCS occurrence.

All regions except for the Central United States experience an increase in MCS frequency in the future period (Supplementary Fig. 2), which is in agreement with previous studies that show an increase in convective extremes in future climates^{16,17}. In the Central United States, MCSs with maximum hourly precipitation (P_{\max}) < 40 mm h⁻¹ reduce by 30%, but extreme MCSs with P_{\max} > 90 mm h⁻¹ increase by 380%. Similar high increases in extreme MCSs can be found in other regions. The highest relative increases in MCS frequency occur in Canada and the US Northeast, where MCSs with P_{\max} > 80 mm h⁻¹ are almost unrepresented in the current climate and become frequent in the future (Supplementary Table 1).

P_{\max} of future MCSs shows relative increases of 25% to 40% in northern regions such as Canada, the US Northeast and the US Mid-Atlantic and ~15–20% elsewhere (Supplementary Fig. 3), which is consistent with expectations from the CC relationship because of a greater temperature increase at high latitudes⁴. Also, MCS sizes systematically increase in all regions with the largest increases in southern regions and smaller increases in mid and high latitudes. A significant increase in the convective available potential energy (CAPE)^{18,19} makes the future environment more favourable for convection and allows MCSs to grow larger¹⁴. The combined effect of higher P_{\max} and larger MCSs results in a significant increase in the MCS hourly total rainfall (P_{total}), which is the total volume of precipitation from a system within an hour. Increases in P_{total} range between 20% and 40% in the mid- and high-latitude regions and between 40% and 80% in lower latitudes.

The impact of future MCSs will strongly depend on the combined effect of these changes. MCSs that have high P_{total} relative to

their size rapidly increase in frequency (Fig. 2a), which results in a higher flood potential because of the concentration of large precipitation volumes over small areas. Systems with a high P_{total} and a high P_{\max} also significantly increase in the future climate; however, the largest flood risk occurs from MCSs with a high P_{total} and a slow storm motion. This category of MCSs shows the highest increase in all regions (Fig. 2c), but changes in storm speed are regionally variable. MCSs that move slower than 20 km h⁻¹ reduce their speed by up to 20% in the US Midwest and Mid-Atlantic, and in Canada, but are faster in Mexico and the US Northeast (Supplementary Fig. 3). Changes in the MCS motion are consistent with changes in the steering level flow (~7 km wind speed²⁰ (Supplementary Fig. 4)) and changes in MCS internal processes such as cold pool dynamics¹⁴.

Next, changes in the 40 MCSs with the highest P_{\max} are investigated in the densely populated US Mid-Atlantic region. For statistical robustness, 40 MCSs were selected and the results do not change significantly for sample sizes between 20 and 100 MCSs. Future MCSs significantly increase their P_{\max} and have substantially larger areas covered by high rain rates (Fig. 3a,b). Mean rain rates are exponentially decreasing with increasing distance from the location of P_{\max} (Fig. 3c), which can be described by the statistical model $P_x = P_{\max} e^{-x/k} + d$ with $d \ll P_{\max}$. Here, x (km) is the distance from the location of P_{\max} , d (mm h⁻¹) is the average rainfall at 80 km distance from P_{\max} and k (km) is the horizontal length scale that denotes the distance from P_{\max} at which $P_x = P_{\max}/2$. On average, P_{\max} increases by 30% from 95 ± 12 mm h⁻¹ to 122 ± 14 mm h⁻¹ (± 1 s.d.), in line with the CC relationship. d is approximately 2.5 ± 1.7 mm h⁻¹ and stays constant in future climates, whereas k significantly increases from 8.1 ± 2.2 km to 9.8 ± 2.6 km. The larger k values cause rainfall to increase from 30% at the location of P_{\max} to ~70% at a radius of 10–30 km around P_{\max} . This substantially increases P_{total} because MCS precipitation volume increases with the square of the distance (Fig. 3d). P_{total} increases are largest on the scale of major cities (O 1,000 km (Fig. 3d)). For example, P_{total} increases by 60% or $3,900 \text{ m}^3 \text{ s}^{-1}$ on the area of New York City, which is equivalent to adding six times the Hudson River discharge to an extreme MCS of the current climate. One-third of the increase in P_{total} is related

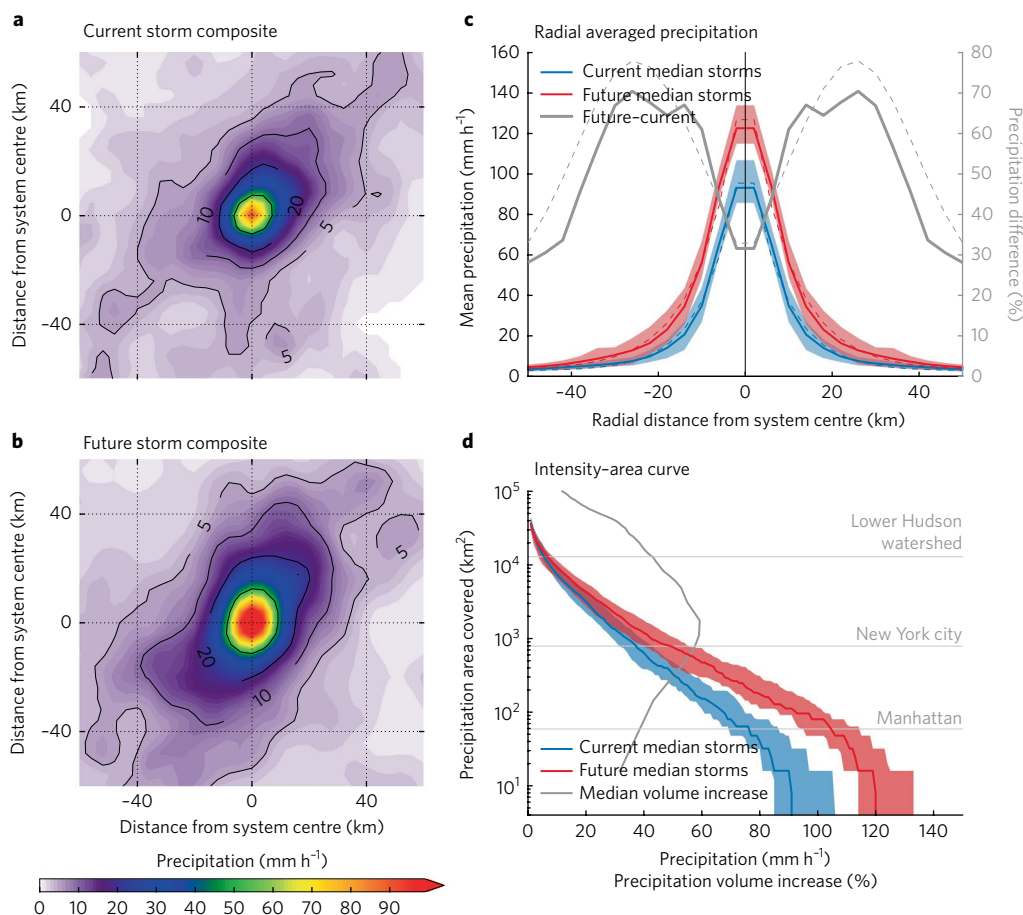


Fig. 3 | Precipitation in the 40 MCSs with highest P_{\max} in the mid-Atlantic region. **a, b**, Hourly MCS precipitation averages at the time of P_{\max} in the current (**a**) and future (**b**) climates composited according to the location of P_{\max} . **c**, Mean rain rates at different radial distances from the location of P_{\max} for current (blue) and future (red) MCSs. Median relative differences are shown in grey and correspond to the secondary y axis. Dashed lines show fitted exponential functions. **d**, Intensity–area curves that show the area covered by certain precipitation rates. The grey line shows relative changes in the precipitation volume relative to spatial scales. In **c** and **d**, the shaded areas correspond to the interquartile range of the 40 MCSs.

to a larger P_{\max} and two-thirds to larger k values. Similar changes are found in Mexico and the US Southeast, North-Atlantic and Midwest regions (Supplementary Fig. 5). Increases in k are not significant and contribute less than 50% to the volume increase in the other regions (Supplementary Fig. 6). The increases in future MCS precipitation volume are consistent with previous studies that focus on individual MCS cases^{21,22}.

To understand the processes that cause the intensification and broadening of heavy precipitation in future MCSs during JJA, we analyse changes in the MCS environments and dynamics (Fig. 4). The future US Mid-Atlantic MCSs have, on average, a 1.8 km higher cloud top that is 3.8 °C colder than in the current climate (Fig. 4a,b and Supplementary Fig. 7). A 10 °C warmer equivalent potential temperature in the boundary layer combined with a higher tropopause lead to a significantly higher CAPE. However, these future environments have larger absolute values of convective inhibition (CIN) of the inflow air (Fig. 4e,f).

The increased CAPE is consistent with an increase of future maximum updraft velocities and mean updraft sizes above 2 km (Supplementary Fig. 7), which is roughly the height of the level of free convection. The stronger updrafts produce more graupel and hail in the core of future MCSs above the future freezing level (Fig. 4c). The fall speed of graupel and hail are at least twice those of snow and ice, which increases the downward fluxes of moisture in future MCSs (Fig. 4d). The downdrafts intensify and broaden, probably in response to enhanced cooling through melting in the warm

cloud layer (between the lifting condensation level and the freezing level) because of an increased input of frozen particles from aloft (Supplementary Fig. 7) and a larger precipitation loading²³.

Figure 4c,d shows that the increase in surface precipitation rates results from a more than 30% increase in downward moisture flux and constant hydrometeor mixing ratios below 2 km height. At higher levels, the largest changes occur for the snow mixing ratio with decreases below 7 km and increases above because of the increased upward moisture transport. The decreases are related to the higher freezing level that leads to an earlier melting of frozen particles and results in an increase of liquid particles of up to 5 g kg⁻¹ (300%) at ~4 km height (Fig. 4c and Supplementary Fig. 8). As raindrops fall ten times faster than ice and snow²⁴, they reside for a shorter period in the atmosphere, which contributes to the enhance downward moisture flux²⁵. Relative humidity is slightly decreased by 1.5% at all levels and the atmosphere becomes more stable because of a 3 °C larger temperature increase in the upper troposphere compared with the near-surface levels (Supplementary Fig. 7). Wind-shear changes are small and have minor effects on the changes in MCS dynamics (Supplementary Fig. 9). Changes in future MCSs in other regions are similar.

The increasing size of MCSs is in line with previous findings that show that large systems are related to high CAPE values¹⁴ and that CAPE is expected to increase because of climate change^{18,19} as a result of a boundary layer that is warmer with increased humidity throughout its depth. Future US Mid-Atlantic MCSs have a 70 m higher lifting condensation level (cloud base) and an 860 m higher

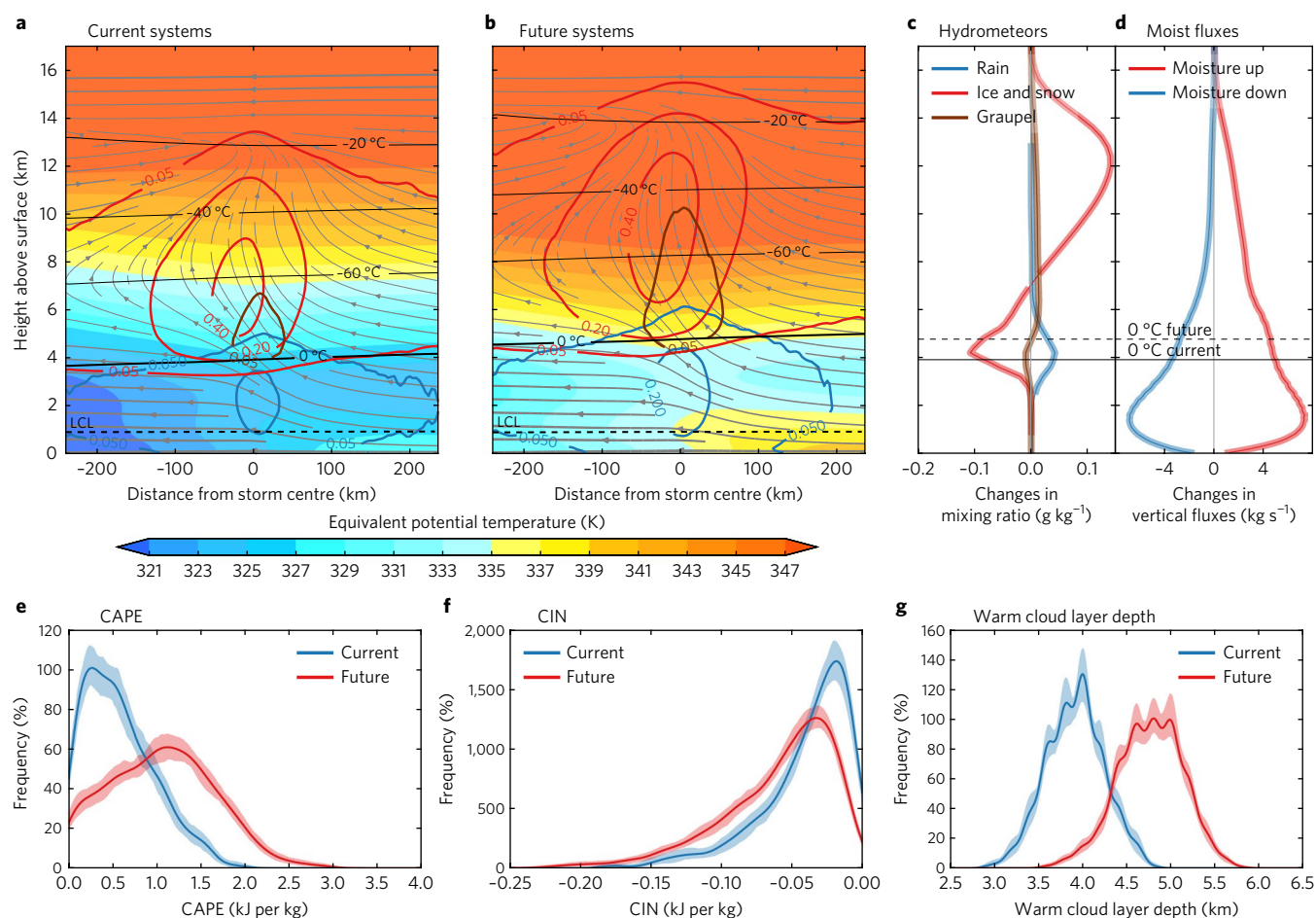


Fig. 4 | Current and future MCSs environments. **a, b**, Average cross-section of the equivalent potential temperature (filled contour), hydrometeor mixing ratios (blue, brown and red contours show rain and cloud, graupel and snow, and ice-mixing ratios, respectively), and wind field (streamlines) relative to the MCS movement for 807 current (**a**) and 1,207 future hourly time slices of mid-Atlantic MCSs (**b**). Black solid lines show isothermals and the black dashed line shows the lifting condensation level (LCL, that is, the cloud base). **c, d**, Average changes (future minus current) in hydrometeor mixing ratios (**c**) and vertical moisture flux (**d**) (upward/downward fluxes are shown as red/blue lines) at different heights above surface. Thick lines show significant changes (alpha is 0.01) according to 100 bootstrap samples. **e–f**, Probability density functions of CAPE (**e**), CIN (**f**) and warm cloud layer depth (**g**) for current (blue) and future (red) MCSs. Shaded areas show the 1–99 percentile range of 100 bootstrap samples. Changes in CAPE and CIN are calculated in the MCS inflow region.

freezing level, which leads to a deepening of the warm cloud layer from 3.2 ± 0.4 km in the current to 4.0 ± 0.4 km in the future climate (Fig. 4g). The deeper layer allows for more precipitation particles to grow via collision and coalescence (warm rain process), which forms larger drops that fall faster and have a greater chance of reaching the surface and contribute to the increase in areas with high rainfall rates. Flash-flood situations are typically associated with warm cloud layers deeper than 3–4 km (ref. ²⁶).

The results show that the relative increase of P_{total} exceeds the relative increases of P_{max} in all regions because of an expansion of the area with heavy precipitation in future MCSs. Most of today's climate change assessments do not account for changes in MCS spatial patterns²⁷, which suggests that future flood impacts may exceed current expectations. This study highlights that a process-based assessment is needed that takes different aspects of climate change into account to assess the full spectrum of related impacts.

The presented climate change signals are significantly larger than the natural variability in our current climate simulations that feature active summer seasons, such as 2001, and inactive seasons, such as the drought year of 2012. A remaining caveat is that we cannot assess the effect of climate internal variability and changing atmospheric circulation patterns on our results. Large-scale

dynamics have a strong control on the genesis and development of MCSs. However, there is limited consensus among climate projections on how large-scale dynamics might change in future US summers, whereas there is higher confidence in changes controlled by thermodynamics²⁸.

Methods

Methods, including statements of data availability and any associated accession codes and references, are available at <https://doi.org/10.1038/s41558-017-0007-7>.

Received: 2 May 2017; Accepted: 6 October 2017;
Published online: 20 November 2017

References

- Feng, Z. et al. More frequent intense and long-lived storms dominate the springtime trend in central US rainfall. *Nat. Commun.* **7**, 13429 (2016).
- Topics Geo: Natural Catastrophes 2015 Analyses, Assessments, Positions (Munich Re, 2016).
- Prein, A. F. et al. A review on regional convection-permitting climate modeling: demonstrations, prospects, and challenges. *Rev. Geophys.* **53**, 323–361 (2015).

4. Prein, A. F. et al. Simulating North American mesoscale convective systems with a convection-permitting climate model. *Clim. Dynam.* (in the press); <https://doi.org/10.1007/s00382-017-3947-8>
5. Clark, A. J., Bullock, R. G., Jensen, T. L., Xue, M. & Kong, F. Application of object-based time-domain diagnostics for tracking precipitation systems in convection-allowing models. *Weather Forecast.* **29**, 517–542 (2014).
6. 74-Year List of Severe Weather Fatalities (NOAA, 2016); <http://www.nws.noaa.gov/om/hazstats.shtml>
7. Wasko, C., Sharma, A. & Westra, S. Reduced spatial extent of extreme storms at higher temperatures. *Geophys. Res. Lett.* **43**, 4026–4032 (2016).
8. Karl, T. R. *Global Climate Change Impacts in the United States* (Cambridge Univ. Press, Cambridge, 2009).
9. Trenberth, K. E., Dai, A., Rasmussen, R. M. & Parsons, D. B. The changing character of precipitation. *Bull. Am. Meteorol. Soc.* **84**, 1205–1217 (2003).
10. Westra, S. et al. Future changes to the intensity and frequency of short-duration extreme rainfall. *Rev. Geophys.* **52**, 522–555 (2014).
11. Liu, C. et al. Continental-scale convection-permitting modeling of the current and future climate of North America. *Clim. Dynam.* **49**, 71–95 (2017).
12. Kendon, E. J. et al. Do convection-permitting regional climate models improve projections of future precipitation change? *Bull. Am. Meteorol. Soc.* **98**, 79–93 (2017).
13. Prein, A. F. et al. The future intensification of hourly precipitation extremes. *Nat. Clim. Change* **7**, 48–52 (2017).
14. Houze, R. A. Mesoscale convective systems. *Rev. Geophys.* **42**, RG4003 (2004).
15. Fritsch, J., Kane, R. & Chelius, C. The contribution of mesoscale convective weather systems to the warm-season precipitation in the United States. *J. Clim. Appl. Meteorol.* **25**, 1333–1345 (1986).
16. Diffenbaugh, N. S., Scherer, M. & Trapp, R. J. Robust increases in severe thunderstorm environments in response to greenhouse forcing. *Proc. Natl Acad. Sci. USA* **110**, 16361–16366 (2013).
17. Gensini, V. A. & Mote, T. L. Downscaled estimates of late 21st century severe weather from CCSM3. *Clim. Change* **129**, 307–321 (2015).
18. Trapp, R. J. et al. Changes in severe thunderstorm environment frequency during the 21st century caused by anthropogenically enhanced global radiative forcing. *Proc. Natl Acad. Sci. USA* **104**, 19719–19723 (2007).
19. Roms, D. M., Seeley, J. T., Vollaro, D. & Molinari, J. Projected increase in lightning strikes in the United States due to global warming. *Science* **346**, 851–854 (2014).
20. Carbone, R., Tuttle, J., Ahijevych, D. & Trier, S. Inferences of predictability associated with warm season precipitation episodes. *J. Atmos. Sci.* **59**, 2033–2056 (2002).
21. Lackmann, G. M. The south-central US flood of May 2010: present and future. *J. Clim.* **26**, 4688–4709 (2013).
22. Schumacher, R. S. & Peters, J. M. Near-surface thermodynamic sensitivities in simulated extreme-rain-producing mesoscale convective systems. *Mon. Weather Rev.* **145**, 2177–2200 (2017).
23. Srivastava, R. A model of intense downdrafts driven by the melting and evaporation of precipitation. *J. Atmos. Sci.* **44**, 1752–1774 (1987).
24. Yuter, S. E., Kingsmill, D. E., Nance, L. B. & Löffler-Mang, M. Observations of precipitation size and fall speed characteristics within coexisting rain and wet snow. *J. Applied Meteorol. Clim.* **45**, 1450–1464 (2006).
25. Rasmussen, R. et al. High-resolution coupled climate runoff simulations of seasonal snowfall over Colorado: a process study of current and warmer climate. *J. Clim.* **24**, 3015–3048 (2011).
26. Doswell, C. *Severe Convective Storms* (Springer, New York, 2015).
27. IPCC *Climate Change 2013: The Physical Science Basis* (eds Stocker, T. et al.) (Cambridge Univ. Press, Cambridge, 2014).
28. Shepherd, T. G. Atmospheric circulation as a source of uncertainty in climate change projections. *Nat. Geosci.* **7**, 703–708 (2014).

Acknowledgements

NCAR is funded by the National Science Foundation (NSF) and this work was partially supported by the NSF EASM Grant AGS-1048829, by the US Army Corps of Engineers (USACE) Climate Preparedness and Resilience Program and NCAR's Water System program. We thank the ECMWF and National Climate Data Centre for making available their datasets. Computer resources were provided by the Computational and Information Systems Laboratory (NCAR Community Computing, <http://n2t.net/ark:/85065/d7wd3xhc>).

Author contributions

A.F.P. designed the study, and collected and analysed the data. C.L. and K.I. performed and post-processed the climate simulations. All the authors contributed to the writing process and gave conceptual advice.

Competing interests

The authors declare no competing financial interests.

Additional information

Supplementary information is available for this paper at <https://doi.org/10.1038/s41558-017-0007-7>.

Reprints and permissions information is available at www.nature.com/reprints.

Correspondence and requests for materials should be addressed to A.F.P.

Publisher's note: Springer Nature remains neutral with regard to jurisdictional claims in published maps and institutional affiliations.

Methods

Climate model simulations. The weather research and forecasting model²⁹ Version 3.4.1 was applied with convection-permitting grid spacing (4 km) over a North American domain (Supplementary Fig. 2). The model domain includes $1,360 \times 1,016$ grid points and 51 stretched vertical levels topped at 50 hPa. The main applied model physics schemes are the Thompson aerosol-aware microphysics³⁰, the rapid radiative transfer model³¹, the Yonsei University planetary boundary layer³² and the improved Noah-MP land-surface model³³. Additionally, weak spectral nudging³⁴ of a large wavelength ($\sim 2,000$ km) of the European Centre for Medium-Range Weather Forecasts (ECMWF) Interim Reanalysis (ERA-Interim) temperature, horizontal wind and geopotential height fields is applied above the planetary boundary layer every six hours. More information about the model setting and a basic evaluation of the model performance and climate change signals is given in Liu et al. (2017)⁴.

A horizontal grid spacing of 4 km is widely accepted as the upper limit for convection-permitting simulations that operate without a cumulus parameterization³. However, this grid spacing is too coarse to resolve the full spectrum of turbulent motions and there is no established theory about how turbulence can be parameterized on such scales. Simulations in the European Alps showed that bulk properties, such as area average-precipitation amounts and vertical fluxes, already converged in a 4 km simulation compared with a 500 m simulation; however, the structure of isolated convective cells did not converge³⁵. Simulations of squall lines in the United States showed that models with a 4 km or 1 km horizontal grid spacing underestimate the entrainment of mid-level air into the system, which leads to higher cloud tops, a slower development and more precipitation compared with 250 m-model simulations^{36,37}. The total upward flux of dry air was fairly similar between the 4 km and 250 m simulations. The studies also show that an intermediate grid spacing of 1 km does not necessarily improve the 4 km model results. The usage of a two-moment microphysics scheme, such as that used in this study, generally improves the simulation, but significant uncertainties in the convection-permitting model simulation of updraft intensities associated with microphysics parameterizations have been reported^{38,39}. Apart from these caveats, our 4 km simulation can reproduce many realistic features of MCSs (Supplementary Fig. 1).

Two 13-year long simulations were performed that consisted of a current climate simulation, in which the ERA-Interim⁴⁰ data were downscaled for the period October 2000 to September 2013 and a future, end-of-the-century, high-end emission scenario (RCP 8.5) climate simulation. For the latter simulation, the pseudo-global warming (PGW) approach⁴⁵ was applied, which is identical to the current climate simulations, but the ERA-Interim lateral boundary conditions and sea-surface temperatures were perturbed by a climate change signal. This signal is the average monthly mean climate change signal of 19 CMIP5 (ref. 41) global circulation models (GCMs) for the periods 1976–2005 and 2071–2100. The PGW approach allows the calculation of representative climate change signals that are related to thermodynamic processes, lapse rate and baroclinicity with the year-to-year variability and large-scale weather patterns largely unaffected. This has the advantage that climate change signals can be attributed to forced climate change processes because the internal climate variability is negligible. The drawback of the PGW approach is that systematic changes in the large-scale circulation are not considered. For instance, dynamic changes in the US nocturnal low-level jet, which is related to MCS intensities and frequency⁴ because of its transports of unstable warm and moist air from the Gulf of Mexico into the Great Plains, might not be fully captured. A recent study⁴² shows the suitability of the PGW approach as it demonstrates that the full climate change signal from a GCM-driven RCM simulation can be decomposed in three additive terms: (1) a large-scale thermodynamic effect, (2) a lapse-rate effect and (3) a large-scale circulation change.

Tracking of convective systems. The storm tracking is performed using the method for object-based diagnostic evaluation (MODE)^{43,44}, which incorporates the time dimension (MODE time-domain or short MTD⁴). This method is based on a four-step approach to identify MCSs. Gridded, hourly accumulated precipitation is smoothed with a square moving window having a side length of eight grid cells. The smoothed field is masked by applying a precipitation threshold of 5 mm h^{-1} , which results in the exclusion of most of the stratiform rain areas and helps focus only on the regions of high rain rate. The masked field is applied to the original hourly precipitation field to obtain precipitation objects. An object is defined as a spatial and temporal contiguous precipitation region with a minimum size of 2,000 grid cells, which results in the detection of moderate- to large-scale MCSs. MTD is able to incorporate merging or splitting of precipitation regions. As output, MTD provides MCS characteristics, such as MCS size, intensity, track, speed or total precipitation.

Statistical analysis. We divided our model domain into seven climate subregions: Mexico, the US Southwest, Southeast, Midwest, Mid-Atlantic and Northeast, and Canada (Supplementary Fig. 2). The regions were selected to account for coherent structures in convective-system climate change signals and were also used for the evaluation of convective systems in the current climate simulations⁵. MCSs are assigned to a subregion according to their centre of hourly precipitation and therefore can be in multiple regions during their lifetime. The track-density

differences shown in Supplementary Fig. 2 correspond to the numbers of MCSs that transect 100×100 km grid boxes in the current and future climate during the 13 investigated summer seasons. The binning of MCS P_{max} values between 40 and 90 mm h^{-1} with 10 mm h^{-1} increments was chosen based on the density function of P_{max} (ref. 5) and allows us to differentiate frequency changes in weak to extreme P_{max} MCSs.

For the assessment of statistical significance, block bootstrapping was applied⁴⁵. MCSs are pooled randomly with replacement from the original sample of MCSs until the same number of MCSs as in the original sample is reached. This is repeated 100 times for the current and future climate period, which enables the assessment of statistical significance. Statistical significance is tested with the non-parametric Mann–Whitney U test using a confidence level of 99% (ref. 45).

The conditional distributions of MCS speed, size and P_{max} given a particular MCS hourly total precipitation (P_{total}) shown in Fig. 2a–c were calculated as follows. First, MCSs are binned according to their (P_{total}) values in $1,200 \text{ m}^3 \text{ s}^{-1}$ bin sizes with a $12,000 \text{ m}^3 \text{ s}^{-1}$ window centred on the actual bin value. MCSs in each bin are classified further according to their motion speed in $2 \pm 10 \text{ km h}^{-1}$ bins, their size in $2,500 \pm 12,500 \text{ km}^2$ bins and their P_{max} in $2 \pm 10 \text{ mm h}^{-1}$. For example, the number of MCSs with $24,000 \pm 6,000 \text{ m}^3 \text{ s}^{-1}$ that have a speed of $40 \pm 10 \text{ km h}^{-1}$ is calculated. The overlap over multiple bins improves the signal-to-noise ratio in the calculated distributions. Then, the relative frequency changes of future and current MCSs is calculated for parts of the distribution that had at least five MCSs in both distributions. Block bootstrapping was used to estimate if the two distributions have statistically significant differences.

For the climate change analysis of the 40 MCSs with highest P_{max} in Fig. 3, we composited MCSs centred on the location of P_{max} at the time of P_{max} and calculated the mean over the hourly precipitation at each grid cell. The average rainfall dependent on the distance to P_{max} was calculated by averaging over precipitation in radial bands of 4 km width. The intensity–area curves were calculated by accumulating the area that is covered by precipitation from highest to lowest precipitation rates for each of the 40 MCSs in the current and future periods. Then, the median of the covered area was calculated for all intensities. The MCS precipitation fields have not been rotated to account for the different orientation of MCSs to avoid interpolation errors, especially the smoothing of precipitation maxima. Rotating the MCSs according to their inflow direction leads to similar results.

Owing to data storage constraints, the 3D model output was saved only every 3 h. Only MCSs that lasted longer than 3 h were included to sample mature systems. The vertical cross-sections of MCSs shown in Fig. 4 were derived by selecting a square box of length 121 grid cells centred around the MCS centre (centre of precipitation of MTD). Thereafter, the data were remapped to a common vertical grid of constant height above ground levels using bilinear interpolation. The lowest level is at $z = 20 \text{ m}$ (the lowest model level) and the vertical grid spacing (Δz) is 100 m from $z = 100$ to 3,000 m. Between 3,000 m and 6,800 m, Δz is 200 m, and between 6,800 m to the highest model level at 26,800 m, Δz is 400 m. The MCS is horizontally rotated such that the MCS inflow/outflow is approximately parallel to the x axis. This is done by calculating the direction of the strongest horizontal equivalent potential temperature gradient in the average lowest three vertical levels. This approach is adopted from studies by Trier et al.^{46,47}. An example of a rotated MCS is shown in Supplementary Fig. 1. After the rotation, all the variables are averaged perpendicular to the inflow direction (along the y axis) of the rotated MCS. This approach allows us to sample a large number of MCSs in a systematic way to construct an average convective-system environment for current and future MCSs.

Additional MCS properties were calculated as follows. The wind speed and direction in hodographs are horizontal averages at each vertical level. The updraft/downdraft size in MCSs are determined by the area in which vertical wind speeds are larger/smaller than $\pm 3.5 \text{ m s}^{-1}$. Clouds are defined as grid cells in which the total mixing ratio of hydrometeors is larger or equal to 0.01 g kg^{-1} , which is used in the calculation of cloud top heights. Convective potential available energy and CIN correspond to the average air properties in the lowest 100 hPa above the surface. They were calculated for every second grid cell in the inflow environment (80 km to 240 km upstream of the MCS centre) in the rotated coordinate system and averaged afterward.

Code availability. The source code of MTD is part of the Developmental Testbed Center's (DTC) Model Evaluation Tools (MET) software and freely available online at <http://www.dtcenter.org/met/users/downloads/>. The code for the statistical analysis is available from the corresponding author on request.

Data availability. The datasets generated and analysed during the current study are available from NCAR's Research Data Archive⁴⁸.

References

- Skamarock, W. C. & Klemp, J. B. A time-split nonhydrostatic atmospheric model for weather research and forecasting applications. *J. Comput. Phys.* **227**, 3465–3485 (2008).
- Thompson, G. & Eidhammer, T. A study of aerosol impacts on clouds and precipitation development in a large winter cyclone. *J. Atmos. Sci.* **71**, 3636–3658 (2014).

31. Iacono, M. J. et al. Radiative forcing by long-lived greenhouse gases: calculations with the AER radiative transfer models. *J. Geophys. Res. Atmos.* **113**, D13103 (2008).
32. Hong, S.-Y., Noh, Y. & Dudhia, J. A new vertical diffusion package with an explicit treatment of entrainment processes. *Mon. Weather Rev.* **134**, 2318–2341 (2006).
33. Niu, G.-Y. et al. The community Noah land surface model with multiparameterization options (Noah-MP): 1. Model description and evaluation with local-scale measurements. *J. Geophys. Res. Atmos.* **116**, D12109 (2011).
34. von Storch, H., Langenberg, H. & Feser, F. A spectral nudging technique for dynamical downscaling purposes. *Mon. Weather Rev.* **128**, 3664–3673 (2000).
35. Langhans, W., Schmidli, J. & Schär, C. Bulk convergence of cloud-resolving simulations of moist convection over complex terrain. *J. Atmos. Sci.* **69**, 2207–2228 (2012).
36. Bryan, G. H. & Morrison, H. Sensitivity of a simulated squall line to horizontal resolution and parameterization of microphysics. *Mon. Weather Rev.* **140**, 202–225 (2012).
37. Lebo, Z. & Morrison, H. Effects of horizontal and vertical grid spacing on mixing in simulated squall lines and implications for convective strength and structure. *Mon. Weather Rev.* **143**, 4355–4375 (2015).
38. Varble, A. et al. Evaluation of cloud-resolving and limited area model intercomparison simulations using TWP-ICE observations: 1. Deep convective updraft properties. *J. Geophys. Res. Atmos.* **119**, D12206 (2014).
39. Fan, J., Wang, Y., Rosenfeld, D. & Liu, X. Review of aerosol–cloud interactions: mechanisms, significance, and challenges. *J. Atmos. Sci.* **73**, 4221–4252 (2016).
40. Dee, D. et al. The ERA-Interim reanalysis: configuration and performance of the data assimilation system. *Q. J. R. Meteorol. Soc.* **137**, 553–597 (2011).
41. Taylor, K. E., Stouffer, R. J. & Meehl, G. A. An overview of CMIP5 and the experiment design. *Bull. Am. Meteorol. Soc.* **93**, 485–498 (2012).
42. Kröner, N. et al. Separating climate change signals into thermodynamic, lapse-rate and circulation effects: theory and application to the European summer climate. *Clim. Dynam.* **48**, 3425–3440 (2017).
43. Davis, C., Brown, B. & Bullock, R. Object-based verification of precipitation forecasts. Part I: Methodology and application to mesoscale rain areas. *Mon. Weather Rev.* **134**, 1772–1784 (2006).
44. Davis, C. A., Brown, B. G., Bullock, R. & Halley-Gotway, J. The method for object-based diagnostic evaluation (MODE) applied to numerical forecasts from the 2005 NSSL/SPC Spring Program. *Weather Forecast.* **24**, 1252–1267 (2009).
45. Wilks, D. S. *Statistical Methods in the Atmospheric Sciences* Vol. 100 (Academic, Oxford, 2011).
46. Trier, S. B., Davis, C. A., Ahijevych, D. A. & Manning, K. W. Use of the parcel buoyancy minimum (B min) to diagnose simulated thermodynamic destabilization. Part I: Methodology and case studies of MCS initiation environments. *Mon. Weather Rev.* **142**, 945–966 (2014).
47. Trier, S. B., Davis, C. A., Ahijevych, D. A. & Manning, K. W. Use of the parcel buoyancy minimum (B min) to diagnose simulated thermodynamic destabilization. Part II: Composite analysis of mature MCS environments. *Mon. Weather Rev.* **142**, 967–990 (2014).
48. *High Resolution WRF Simulations of the Current and Future Climate of North America* (NCAR, accessed 5 August 2017); <https://rda.ucar.edu/datasets/ds612.0/>